Journal of Structural Geology 32 (2010) 136–150

Contents lists available at ScienceDirect

Journal of Structural Geology

journal homepage: www.elsevier.com/locate/jsg

Determination of amphibole fracture strength for quantitative palaeostress analysis using microboudinage structures

Nozomi Kimura [a,*], Shotaro Nakayama [b], Katsuhiro Tsukimura [a], Shinko Miwa [b], Atsushi Okamoto [c], Toshiaki Masuda [b]

[a] AIST, Geological Survey of Japan, Tsukuba 305-8567, Japan
[b] Institute of Geosciences, Shizuoka University, Shizuoka 422-8529, Japan
[c] Graduate School of Environmental Studies, Tohoku University, Sendai 980-8579, Japan

ARTICLE INFO

Article history:
Received 30 June 2008
Received in revised form
26 September 2009
Accepted 14 October 2009
Available online 21 October 2009

Keywords:
Fracture strength
Amphibole
Size effect
Absolute magnitude of palaeodifferential stress
Microboudin

ABSTRACT

The fracture strength of amphibole is estimated with the aim of extending the applicability of the microboudin method to palaeostress analysis. Before estimating the fracture strength of amphibole, it is necessary to evaluate the influence of the size effect on fracturing. Among the three models of size effect (effective-length, effective-area, and effective-volume), the effective-length model is found to be the most suitable in our microboudinage analysis of a metachert from Turkey that contains numerous microboudinaged amphibole grains of variable width embedded within a quartz matrix. Taking into account the influence of the size effect on fracturing, we undertook a comparative microboudinage analysis of the metachert sample, which also contains coexisting microboudinage structures of tourmaline and epidote. The analysis revealed an instantaneous-fracture strength for amphibole of 80 MPa for a 1 mm cube. The far-field differential stress (σ_0), calculated based on amphibole microboudinage structures and considering the effect of the fatigue limit, is $\sigma_0 = 8\lambda(\frac{1}{\overline{w}})^{1/2}$, where λ is the dimensionless stress parameter determined by microboudinage analysis and $\overline{w}$ is the mean width of amphibole grains.

1. Introduction

The nature of palaeostress within orogenic belts is a fundamental parameter in gaining a quantitative understanding of geodynamic processes within the earth; however, there exists no reliable and practical method for estimating the components of the absolute magnitude of the palaeostress tensor. In the 1970s, three metallurgical methods of stress analysis were introduced, based on grain size, subgrain size, and dislocation density; these methods have since been widely used to estimate palaeodifferential stress during plastic deformation within orogenic belts (e.g., Mercier et al., 1977; Twiss, 1977, 1986; Weathers et al., 1979; Kohlstedt and Weathers, 1980; Ord and Christie, 1984; Küster and Stöckhert, 1999; Stipp and Tullis, 2003). These metallurgical methods assume steady-state deformation and no post-tectonic annealing, which are likely to be invalid assumptions when considering orogenic processes (e.g., White et al., 1980; Passchier and Trouw, 2005; Masuda et al., 2007). Methods based on calcite twins and microboudins have subsequently been proposed for palaeostress analysis based on observations of microstructures in deformed rocks (e.g., Jamison and Spang, 1976; Masuda et al., 1989, 2003; Burkhard, 1993; Kimura et al., 2006; Lacombe, 2007). The advantage of these methods is their applicability to cases involving non-steady-state deformation.

The microboudin method is based on the proportion of boudinaged mineral grains with respect to applied differential stress. As this proportion is not linearly related to the applied stress, the method involves some complexities. In the microboudin method, it is essential to determine the magnitude of fracture strength for microboudinaged minerals in estimating palaeodifferential stress (e.g., Masuda et al., 2003). Kimura et al. (2006) experimentally determined the magnitude of instantaneous-fracture strength for tourmaline and epidote, meaning that these two minerals can now be used for quantitative palaeostress analysis. Amphibole is also a potentially useful mineral for microboudinage analysis because it is a common rock-forming mineral (e.g., Ernst, 1968; Leake, 1968; Papike, 1969; Veblen, 1981); however, the fracture strength of amphibole has yet to be determined experimentally because of difficulties in preparing amphibole specimens of treatable size.

* Corresponding author.
E-mail address: kimura-nonn@aist.go.jp (N. Kimura).

0191-8141/$ – see front matter © 2009 Elsevier Ltd. All rights reserved.
doi:10.1016/j.jsg.2009.10.008

With the aim of enabling the use of amphibole microboudins in palaeostress analysis, the present study quantitatively evaluates the size effect for fracturing in terms of naturally occurring sub-millimetre-scale amphibole grains, and then indirectly determines the fracture strength of amphibole based on coexisting microboudinage structures of sodic amphibole, tourmaline, and epidote in a single sample of naturally deformed metachert from central Turkey.

2. Sample description

The analysed sample is a pebble of metachert collected from a Cretaceous high-pressure metamorphic belt in Eskisehir, central Turkey (e.g., Okay et al., 1998; Okay, 2002). Peak metamorphic conditions for the belt are estimated to have been 430 °C and 2.4 GPa (Okay, 2002). The sample is the same as that described in Masuda et al. (2004b, 2008).

The sample is dominantly composed of quartz, with subordinate sodic amphibole, tourmaline, epidote, garnet, muscovite, apatite, chlorite, and opaque minerals. The sample contains a clearly developed foliation defined by the shape-preferred orientation of muscovite and bands of contrasting colour. A weak lineation upon the foliation surface is defined by the alignment of columnar minerals (sodic amphibole, tourmaline, and epidote). Because the long axes of columnar minerals are variably oriented upon the foliation surface (Fig. 1), the orientation of the lineation is determined using a statistical method (Masuda et al., 1999, 2004b). The calculated orientations of mineral lineations defined respectively by sodic amphibole, tourmaline, and epidote fall within 6. As in Masuda et al. (2004b, 2008), the orientation of the lineation in the present sample is defined by the alignment of sodic amphibole grains. No folding is apparent in the sample.

Columnar mineral grains of amphibole, tourmaline, and epidote are classified into three orientations: *p*- and *c*-orientations, and others. *p*-orientation grains are those with long axes oriented parallel to the lineation (±15°), and *c*-orientation grains are those with long axes oriented perpendicular to the lineation (±15°) (Fig. 1b,c). For a given mineral species, the number of *p*-orientation grains is 4–5 times greater than the number of *c*-orientation grains.

Three columnar minerals (sodic amphibole, tourmaline, and epidote) exhibit microboudinage structures within the quartz matrix of the sample (Fig. 2). The microboudinage structures are similar to those described in previous papers (e.g., Masuda et al., 1989, 1995, 2003, 2004b, 2008), with columnar mineral grains being fractured nearly perpendicular to their long axes and microboudins being pulled apart parallel to the long axes, without any evidence of significant rotation during microboudin development. The lack of rotation indicates that a pure shear component was predominant on the foliation surface, suggesting coaxial bulk deformation during microboudinage: if non-coaxial deformation had been predominant, the boudins would have been arranged asymmetrically (e.g., Goscombe et al., 2004; Passchier and Trouw, 2005). In the following analysis, it is assumed that the maximum principal stress σ_1 acted perpendicular to the foliation, while the minimum principal stress σ_3 acted parallel to the lineation, as shown in Fig. 1a. The pure shear strain during microboudinage in the analysed sample is also discussed in detail in Masuda et al. (2004b).

Amphibole overgrowths occur locally on the fracture plane in the interboudin gap within sodic amphibole crystals (Fig. 2f–h), whereas no overgrowths are apparent within tourmaline or epidote microboudins. Electron probe microanalysis reveals that the host sodic amphibole is mostly glaucophane, while the overgrowth phase is magnesioriebeckite (Masuda et al., 2004b). The amphibole nomenclature employed in the present study follows that of Leake et al. (1997).

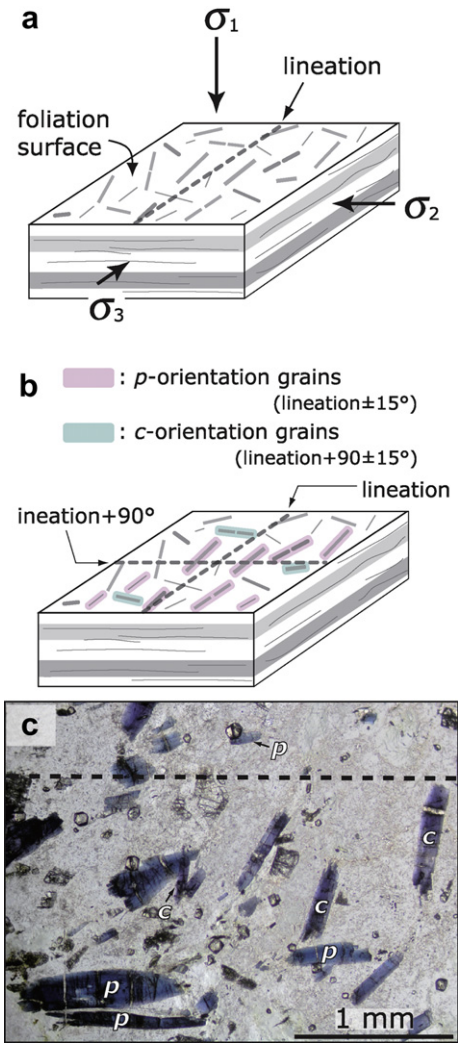

Fig. 1. (a) Schematic of the orientation of the principal stress axes ($\sigma_1 > \sigma_2 > \sigma_3$) acting on the analysed metachert sample at the time of microboudinage. The σ_1 axis is assumed to be perpendicular to the foliation, and the σ_3 axis is parallel to the lineation on the foliation surface. (b) Definition of *p*- and *c*-orientation grains on the foliation surface. *p*-orientation grains (pink) are those with long axes oriented parallel to the lineation (±15°), and *c*-orientation grains (blue) are those with long axes perpendicular to the lineation (±15°). The orientation of the lineation can be determined using a statistical method (Masuda et al., 1999, 2004b). (c) Photomicrograph of the metachert sample on the foliation surface. The orientation of the mineral lineation is indicated by the dashed line. The long axes of sodic amphibole grains are variably oriented. *p*: *p*-orientation grains, *c*: *c*-orientation grains. Plane polarized light. (For interpretation of the references to colour in this figure legend, the reader is referred to the web version of this article.)

3. Principle of size-effect analysis

3.1. Relationship between S^* and λ of different groups of grains

The microboudinage analysis undertaken by Masuda et al. (2003) provides the relationship between the far-field differential stress applied to the sample (σ_0) and the mean fracture strength (the modal-extension fracturing) of the microboudinaged mineral at a unit aspect ratio (S^*):

$$\sigma_0 = \lambda S^*, \quad (1)$$

where λ is the dimensionless stress parameter, which is related to the proportion of microboudinaged grains relative to the total

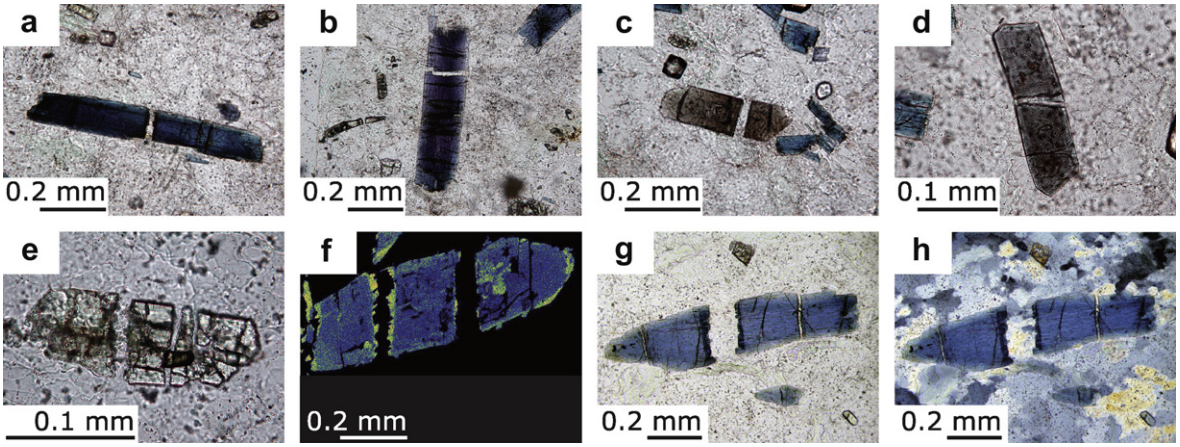

Fig. 2. Photomicrographs of metachert cut parallel to the foliation. In all cases, the orientation of the lineation is parallel to the base of the photomicrograph. (a) *p*-orientation sodic amphibole, (b) *c*-orientation sodic amphibole, (c) *p*-orientation tourmaline, (d) *c*-orientation tourmaline, (e) *p*-orientation epidote. (f) Example of the pattern of Fe zoning within amphibole boudins, as analysed using an EPMA (JEOL 8900) housed at AIST, Japan. The host amphibole is glaucophane, and the amphibole overgrowths in the interboudin gap (yellow–green colour) are magnesioriebeckite. Increasing Fe content is indicated by the gradation from bluish to reddish colours. Black areas are quartz. (g) Photomicrograph of magnesioriebeckite overgrowths (dark blue areas bordering the interboudin gap). Note that there are no overgrowths in the smaller interboudin gaps. Plane polarized light. (h) Same view as in (g), but crossed polarized light. (For interpretation of the references to colour in this figure legend, the reader is referred to the web version of this article.)

number of grains. S^* is influenced by temperature, pressure, size of microboudinaged grains, subcritical crack growth (fatigue), and other possible environmental factors. If the microboudinage analysis is performed separately for groups of grains of contrasting size within a single sample, the size effect can be investigated as follows.

Consider two representative groups (A and B) of sodic amphibole grains. The above relationship can be rewritten as

$$\sigma_0 = \lambda_A S_A^* \tag{2}$$

and

$$\sigma_0 = \lambda_B S_B^*, \tag{3}$$

where the subscripts A and B denote the respective groups. σ_0 has the same value in both of these equations, as the value is given for the metachert sample as a whole. Thus,

$$\lambda_A S_A^* = \lambda_B S_B^* = \sigma_0. \tag{4}$$

In this case, σ_0, S_A^*, and S_B^* cannot be determined independently; instead, the ratio of S_B^* to S_A^* is used, as given by

$$\frac{S_B^*}{S_A^*} = \frac{\lambda_A}{\lambda_B}. \tag{5}$$

3.2. Size-effect models

Three models of the size effect for fracture strength have been proposed based on the weakest-link theory of Weibull (1951): the effective-volume, effective-area, and effective-length models (e.g., Davidge, 1979; Matsuo et al., 1987; Awaji, 2001; Kimura et al., 2006). These models are concerned with the location of critical microcracks that become sites for initial fracture propagation. If such microcracks are found internally within amphibole grains, the effective-volume model is applied; if they are located on the surface of amphibole grains, the fracturing should obey the effective-area model; and if confined to the edges of columnar amphibole grains, the effective-length model is applied.

In the following theoretical analysis, rectangular prisms are assumed for the shape of boudin materials. Before examining the influence of size on the fracture strength of groups A and B (S_A^* and S_B^*), the modal fracture strength of cubic grains with two specific sizes (i.e., cube width) must be considered. S_{w1}^* and S_{w2}^* are defined as the modal fracture strengths for widths of w_1 and w_2 (i.e., widths of microboudins; see Fig. 3a). The relationship between S_{w1}^* and S_{w2}^* is given by the effective-volume model:

$$\frac{S_{w2}^*}{S_{w1}^*} = \left(\frac{V_{w1}}{V_{w2}}\right)^{1/m}, \tag{6}$$

where m is the Weibull modulus, and V_{w1} and V_{w2} are the effective volumes of grains with widths w_1 and w_2, respectively (e.g., Davidge, 1979; Awaji, 2001). The effective-volume at width w_1 can then be calculated by

$$V_{w1} = \int_V \left(\frac{\sigma}{\sigma_{\max}}\right)^{1/m} \mathrm{d}V, \tag{7}$$

where $\sigma_{\max}$ is the maximum differential stress generated in the grains, σ is the differential stress given as a function of location in the grain, and V is a dummy parameter for volume. In this case of microboudinage analysis, σ is approximated by the shear-lag model for fibres, as presented by Zhao and Ji (1997):

$$\sigma = E_f \varepsilon \left[1 - \left(1 - \frac{E_q}{E_f}\right)\frac{\cosh(\delta x)}{\cosh(\delta l)}\right], \tag{8}$$

where E_q and E_f are the elastic constants of the matrix (quartz) and microboudin minerals (amphibole), respectively; ε is the far-field strain; l is the length of the microboudin or intact grain; x is a variable that denotes the location in the grain (Fig. 3b); and δ is expressed as

$$\delta = \frac{2}{w}\left[\frac{E_q}{(1+\upsilon_q)\ln(R/r_0)E_f}\right]^{1/2}, \tag{9}$$

where υ_q is Poisson's ratio for the matrix, and R and r_0 are the mean distance between adjacent fibres (microboudin minerals) and the fibre radius, respectively (Masuda et al., 2003). Although Eq. (8) is not simple, the value of σ is close to that of $\sigma_{\max}$ in the central three-quarters of the grain (Fig. 3b); thus, the assumption that

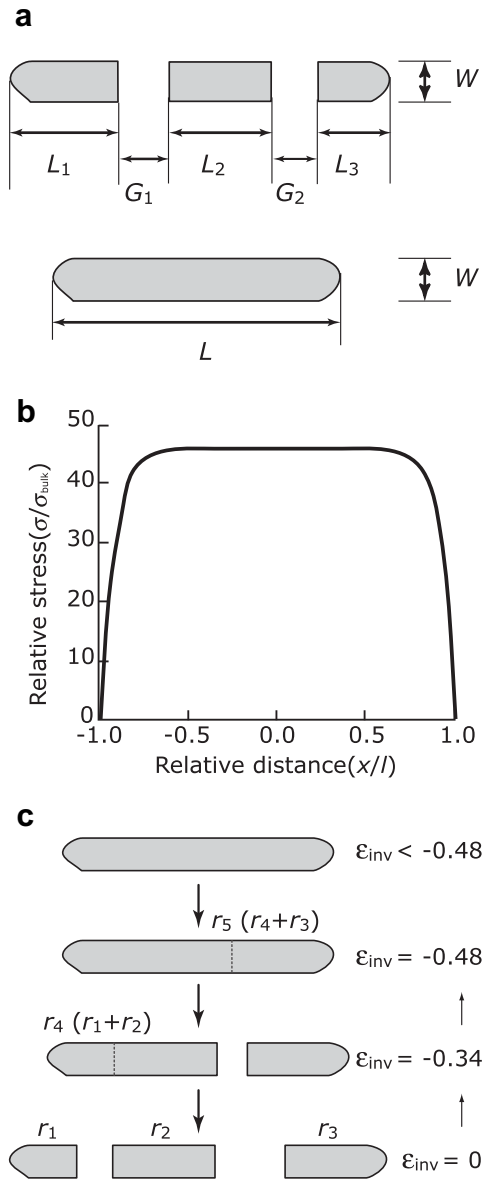

Fig. 3. (a) Definitions of the measured dimensions of microboudinaged (top) and intact grains (bottom). The aspect ratio is calculated as $r = L/W$ (L = length, W = width). L_i and G_i are used to reconstruct the history of microboudinage following the method proposed by Ferguson (1981). (b) Distribution of differential stress (σ) in fibres according to the shear-lag model, after Zhao and Ji (1997). σ_{bulk} is equivalent to the far-field stress, l is the grain length (for both microboudinaged and intact grains), and x is a variable that denotes the location in the grain. The maximum stress occurs at the centre of the grain, but the stress around the central three-quarters of the grain is almost equivalent to the maximum value. (c) Schematic of progressive microboudinage with increasing strain. The bottom figure shows the final microstructure observed under an optical microscope, while the two middle figures show intermediate stages restored using the strain reversal method (e.g., Ferguson, 1981); the top figure shows the original intact grain. Large arrows show the progression of microboudinage, and small arrows show the path of restoration from the present microstructure to the original intact grain. r_1–r_5 are the aspect ratios of the different grains that existed throughout the history of microboudinage. r_4 and r_5 are restored values for grains fractured (microboudinaged) in the past. Values of ε_{inv} represent the strain at which fracturing occurred. In this case, fracturing events occurred at $\varepsilon_{inv} = -0.34$ and -0.48. The treatment of the grains changed on reaching the ε_{inv} values at fracturing. For example, the r_4 grain was fractured at $\varepsilon_{inv} = -0.34$; it was counted as an intact grain at $\varepsilon_{inv} \leq -0.34$ and as a microboudinaged grain at $-0.34 < \varepsilon_{inv}$. For $-0.34 < \varepsilon_{inv}$, the fragments (grains r_1 and r_2) of the microboudin (grain r_4) were newly counted as intact grains. Accordingly, there exist two microboudinaged grains (r_4 and r_5) and 3 intact grains (r_1, r_2, and r_3) when $-0.34 < \varepsilon_{inv}$, one microboudinaged grain (r_5) and 2 intact grains (r_3 and r_4) when $-0.48 < \varepsilon_{inv} \leq -0.34$, and 1 intact grain ($r_5$) when $\varepsilon_{inv} \leq -0.48$.

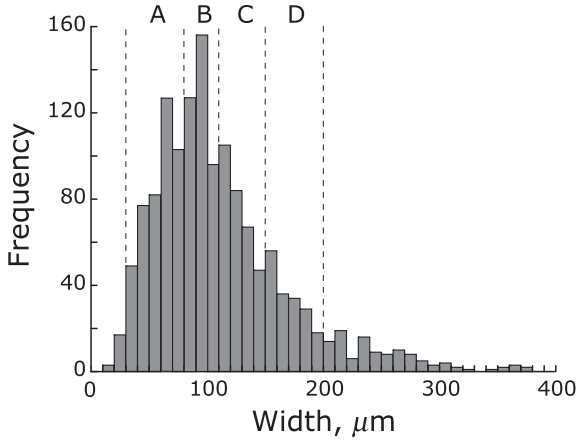

Fig. 4. Frequency distribution of grain widths of sodic amphibole prior to microboudinage. Grains are classified into six groups (*A–D* and two other groups). For details of the groupings, see the main text.

$\sigma/\sigma_{\max} = 1$ in the fibre is considered to be a practical approximation. Equation (7) can therefore be rewritten as

$$V_{w1} = \int_V dV = w_1^3. \tag{10}$$

Similarly,

$$V_{w2} = w_2^3. \tag{11}$$

Thus, Eq. (6) can be replaced by

$$\frac{S^*_{w_2}}{S^*_{w_1}} = \left(\frac{w_1}{w_2}\right)^{3/m}. \tag{12}$$

This equation is pertinent only to grains of width w_1 or w_2. As groups *A* and *B* usually consist of many grains with a range of widths, the values of $S^*_{w_1}, S^*_{w_2}$, w_1, and w_2 are assumed to be replaceable by $S^*_A, S^*_B, \overline{w_A}$, and $\overline{w_B}$, respectively, as given by

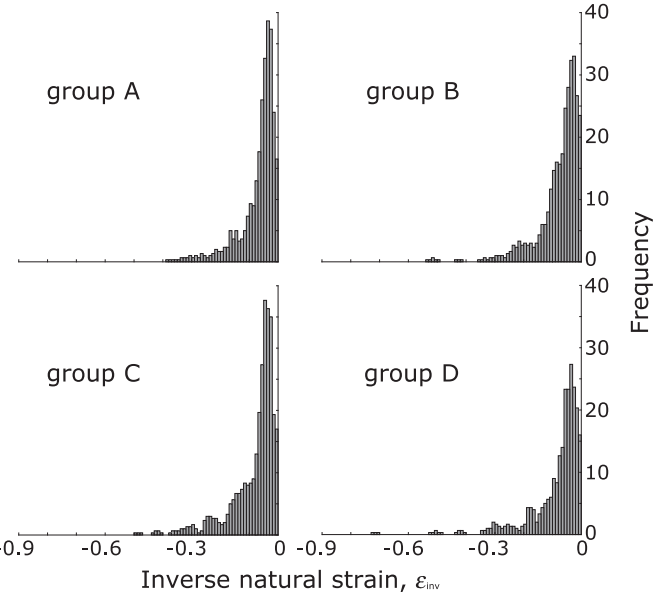

Fig. 5. Frequency distribution of fracturing with respect to inverse natural strain (ε_{inv}, with steps of 0.01) for sodic amphibole in each group of grains.

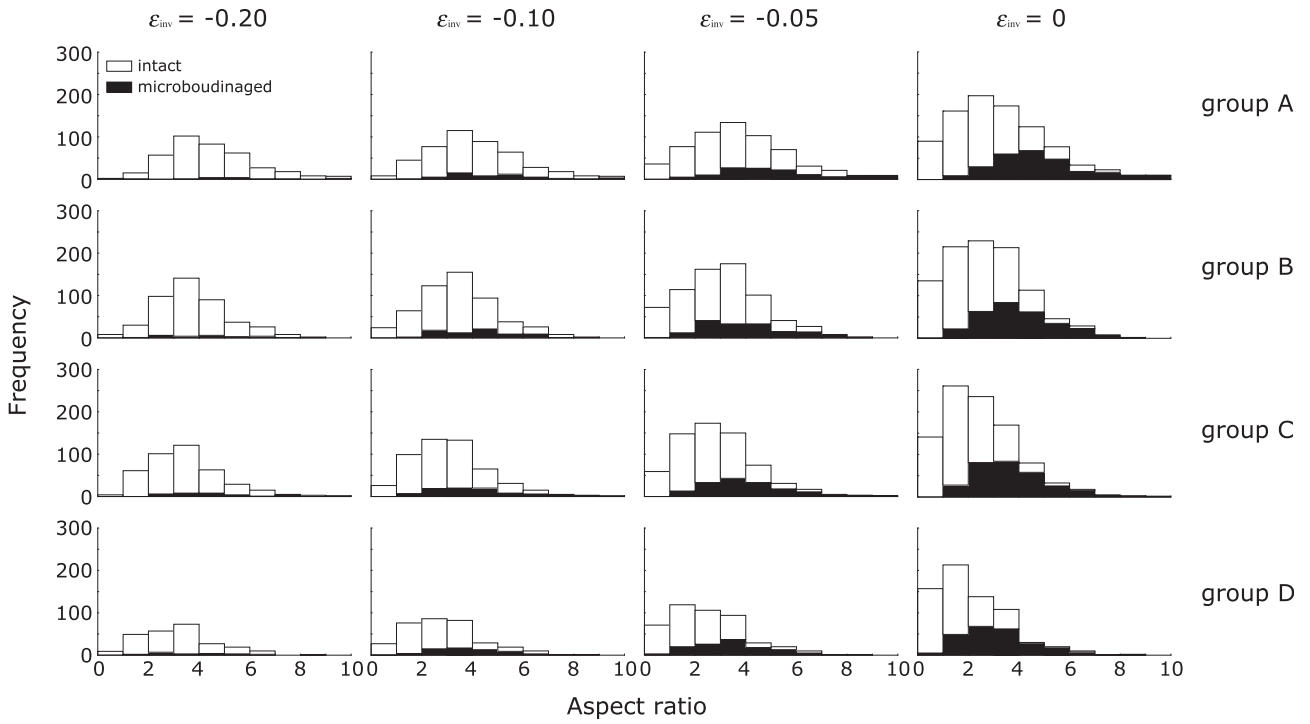

Fig. 6. Frequency distributions of microboudinaged (black) and intact (white) sodic amphibole grains (groups *A*–*D*) with respect to aspect ratio at $\varepsilon_{inv} = 0$, −0.05, −0.10, and −0.20.

$$\frac{S_B^*}{S_A^*} = \left(\frac{\overline{w_A}}{\overline{w_B}}\right)^{3/m}, \tag{13}$$

where S_A^* and S_B^* are representative modal fracture strengths for groups *A* and *B*, respectively, and $\overline{w_A}$ and $\overline{w_B}$ are the geometric means of the widths of each group. For justification of the geometric mean, see Appendix 1.

The relationships according to the effective-area and effective-length models are assumed in a similar manner, as

$$\frac{S_B^*}{S_A^*} = \left(\frac{\overline{w_A}}{\overline{w_B}}\right)^{2/m} \tag{14}$$

and

$$\frac{S_B^*}{S_A^*} = \left(\frac{\overline{w_A}}{\overline{w_B}}\right)^{1/m}, \tag{15}$$

respectively. Thus, Eqs. (13)–(15) can be unified as

$$\frac{S_B^*}{S_A^*} = \left(\frac{\overline{w_A}}{\overline{w_B}}\right)^{z/m}, \tag{16}$$

where $z = 1$, 2, or 3 according to adoption of the effective-length, effective-area, or effective-volume model, respectively.

3.3. Determination of a suitable size-effect model

The following equation can be derived from Eqs. (5) and (16):

$$\frac{\lambda_A}{\lambda_B} = \left(\frac{\overline{w_A}}{\overline{w_B}}\right)^{z/m}. \tag{17}$$

We replace *A* by *X* and *B* by *D* in this equation for the convenience of later analysis:

$$\frac{\lambda_X}{\lambda_D} = \left(\frac{\overline{w_X}}{\overline{w_D}}\right)^{z/m}, \tag{18}$$

which is equivalent to

$$\log\left(\frac{\lambda_X}{\lambda_D}\right) = \frac{z}{m}\log\left(\frac{\overline{w_X}}{\overline{w_D}}\right), \tag{19}$$

where *X* is the dummy suffix denoting *A*, *B*, or *C*. Plotting the values of λ_x, λ_D, $\overline{w_X}$, and $\overline{w_D}$ on a diagram of $\log(\lambda_X/\lambda_D)$ versus $\log(\overline{w_X}/\overline{w_D})$ enables z/m to be calculated. The values of λ_x, λ_D, $\overline{w_X}$, and $\overline{w_D}$ are determined via the microboudinage analysis described below.

4. Analytical procedure of the microboudin technique

The detailed procedure employed in microboudinage analysis is reported in Masuda et al. (1989, 1990, 2003) and Kimura et al. (2006), and is described briefly below.

4.1. Measurement of sodic amphibole morphology

We analysed *p*-orientation sodic amphibole grains (Fig. 1b,c). We measured the lengths and widths of intact grains, and the lengths, widths, and interboudin-gap distances of microboudinaged grains (Fig. 3a).

The morphology of the host amphibole part (glaucophane) is regarded as that of the initial intact grain before microboudinage. Amphibole overgrowths (magnesioriebeckite) were ignored when measuring interboudin gaps between sodic amphibole microboudins, because the overgrowths developed after the opening of the interboudin gap and therefore had no influence on the timing of fracturing.

4.2. Grouping of sodic amphibole grains

The distribution of grain widths for sodic amphibole (Fig. 4) is used as the basic data for the size-effect analysis. The grains are

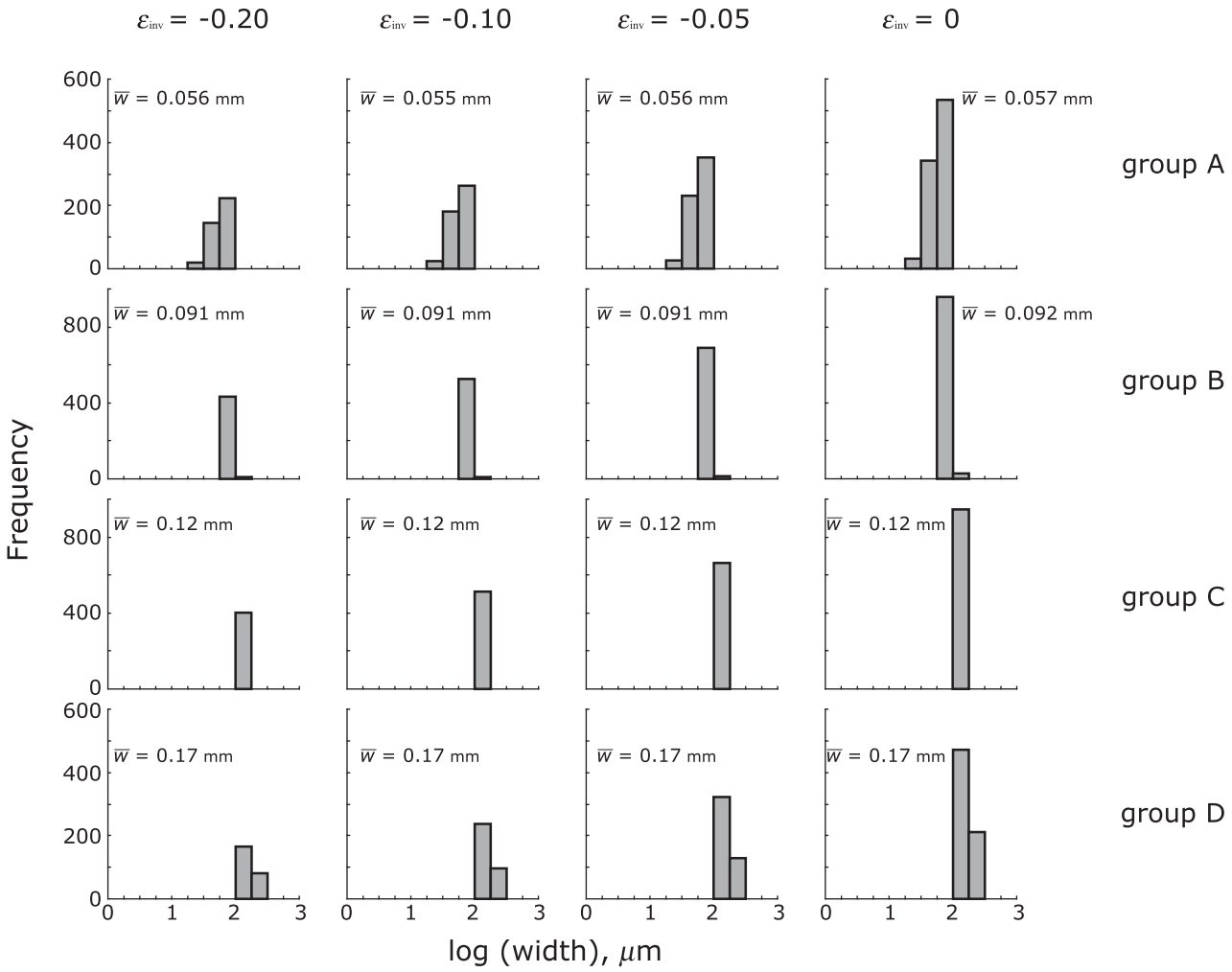

Fig. 7. Frequency distributions of the width of sodic amphibole grains (groups *A*–*D*) at $\varepsilon_{inv} = 0$, −0.05, −0.10, and −0.20. $\overline{w}$ indicates the geometric mean width of the grains.

classified into six groups (*A*–*D* and two other groups) with respect to width (Fig. 4), and the data for groups *A*–*D* are used for the size-effect analysis. The critical widths that represent the boundaries between neighbouring groups for groups *A*–*C* are chosen arbitrarily such that similar numbers of grains (∼350) are assigned to each of the three groups. The range of widths for group *D* is taken such that it occupies the same interval as that for group *A*. Grains of >200 μm in width are not considered in this analysis, as the range would then be too wide; grains of <30 μm in width are also not considered, as the number of grains of this size is too small to yield reliable data from the analysis.

4.3. Reconstruction of microboudinage history

All grains that existed during the period of microboudinage were restored to their pre-boudinage shapes using the strain reversal method (Ferguson, 1981; Lloyd and Condliffe, 2003), which gives the partial plastic natural-log strain of the matrix (metachert in the present study) between the stage at which fracturing occurred in a given columnar grain and the stage at which the matrix material (quartz in the present study) ceased to deform plastically (Fig. 3c). The plastic strain of the matrix is represented by ε_{inv}, which is scaled toward the past; i.e., the cessation of plastic deformation of the matrix corresponds to $\varepsilon_{inv} = 0$, and ε_{inv} at the time of fracturing has a negative value. The practical procedure to be followed is described in the caption to Fig. 3c. The strain reversal method provides the frequency distribution of fracturing with respect to ε_{inv} (Fig. 5). These data are used to restore the frequency distributions of microboudinaged and intact grains with respect to aspect ratio, as described below. The distribution shown in Fig. 5 is plotted as a moving average (window size, 0.03 ε_{inv}) to visually enhance the distinctions between different distribution patterns.

4.4. Frequency distribution of the aspect ratio and the width of microboudinaged and intact grains at a given value of ε_{inv}

In the microboudinage analysis, fragments of microboudins were counted as newly formed intact grains; thus, the frequency of microboudinaged and intact grains changes across the time points (ε_{inv}) of fracturing (a specific example is described in the caption to Fig. 3c). Figs. 6 and 7 show the frequency distribution of the aspect ratio and width data, respectively, for the four groups (*A*–*D*) of sodic amphibole grains at four representative values of ε_{inv} (0, −0.05, −0.10, and −0.20). In the present study, the geometric mean width is used for $\overline{w}$ (Appendix 1).

4.5. Determination of the stress parameter (λ)

The ratio of the number of microboudinaged grains to the total number of grains (i.e., both microboudinaged and intact) with respect to aspect ratio is fundamental to microboudinage palaeostress analysis. The measured proportion of microboudinaged grains ($M(r)$), as calculated from the data in Fig. 6, is plotted as solid

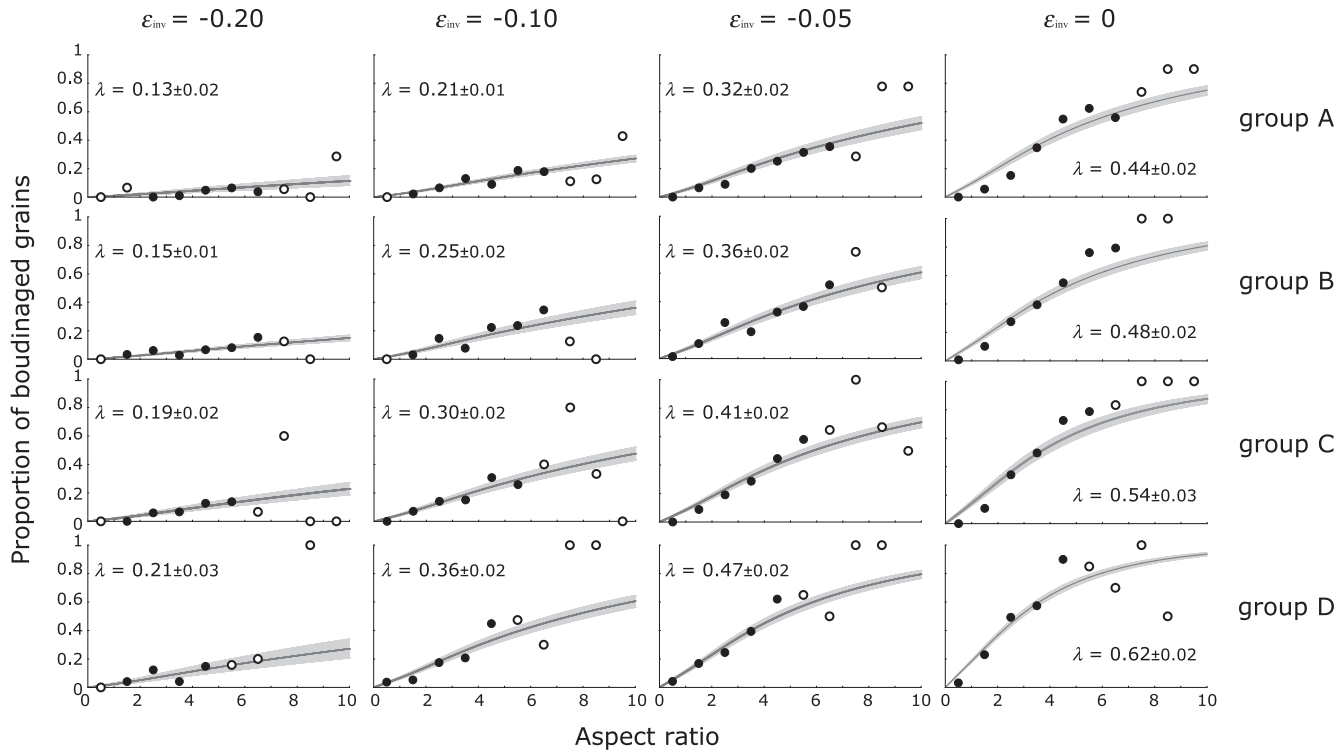

Fig. 8. Proportion of microboudinaged grains (relative to the total number of grains) with respect to aspect ratio and theoretically predicted best-fit curves at $\varepsilon_{inv} = 0$, -0.05, -0.10, and -0.20. Solid and open circles represent reliable ($\geq$25 measured grains) and less reliable ($<$25 measured grains) data, respectively. Solid lines and shaded areas represent the best-fit theoretical curve ($G(r,\lambda)$) and its range of one standard deviation, respectively. Also shown are the values of λ and its standard deviation for sodic amphibole in each group.

circles in Fig. 8. The stress parameter λ, expressed by Eq. (1), is determined by a comparison of the theoretically predicted proportion of microboudinaged grains $G(r,\lambda)$ with the measured proportion $M(r)$. The values of $G(r,\lambda)$ and $M(r)$ are dependent on the aspect ratio r. $G(r,\lambda)$ is described by

$$G(r,\lambda) = 1 - \exp\left[-\frac{m-1}{m} r\lambda^m \left(\frac{E_f}{E_q}\right)^m \times \left\{1 - \left(1 - \frac{E_q}{E_f}\right)\frac{1}{\cosh(A_0 r)}\right\}^m\right], \quad (20)$$

where m is the Weibull modulus; E_f and E_q are the elastic constants of the microboudinaged minerals and matrix mineral (quartz), respectively; and A_0 is a constant (for the derivation of Eq. (20), see Masuda et al., 2003). For sodic amphibole, $m = 2$ is used on the basis of a previous analysis of the samples considered in the present study (Masuda et al., 2004b); the same value has been experimentally determined for tourmaline and epidote (Kimura et al., 2006). For amphibole, we use an E_f/E_q value of 1.2 and an A_0 value of 0.6. These constants are calculated based on the elastic data tabulated in Simmons and Wang (1971).

The sum of the square difference between $M(r_i)$ and $G(r_i,\lambda)$ is defined as a function of λ:

$$T(\lambda) = \sum_{i=1}^{N} h(r_i)[M(r_i) - G(r_i,\lambda)]^2, \quad (21)$$

where $h(r_i)$ is the total number of measured grains at each r_i; $M(r_i)$ and $G(r_i,\lambda)$ are $M(r)$ and $G(r,\lambda)$ for the measurement point (i),

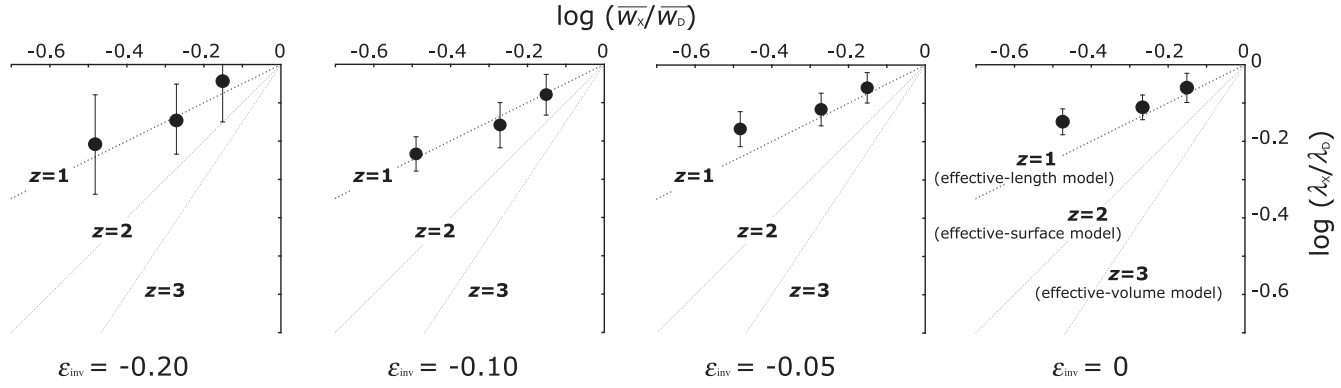

Fig. 9. Diagram of $\log(\lambda_X/\lambda_D)$ versus $\log(\overline{w_X}/\overline{w_D})$ for sodic amphibole grains at $\varepsilon_{inv} = 0$, -0.05, -0.10, and -0.20. The suffix X denotes A, B, or C. The slope in the figure is equivalent to z/m of Eq. (19). Thus, the lines for $z = 3$, 2, and 1 correspond to the effective-volume, effective-surface, and effective-length models for fracturing, respectively. The effective-length model is the most suitable for the plotted data.

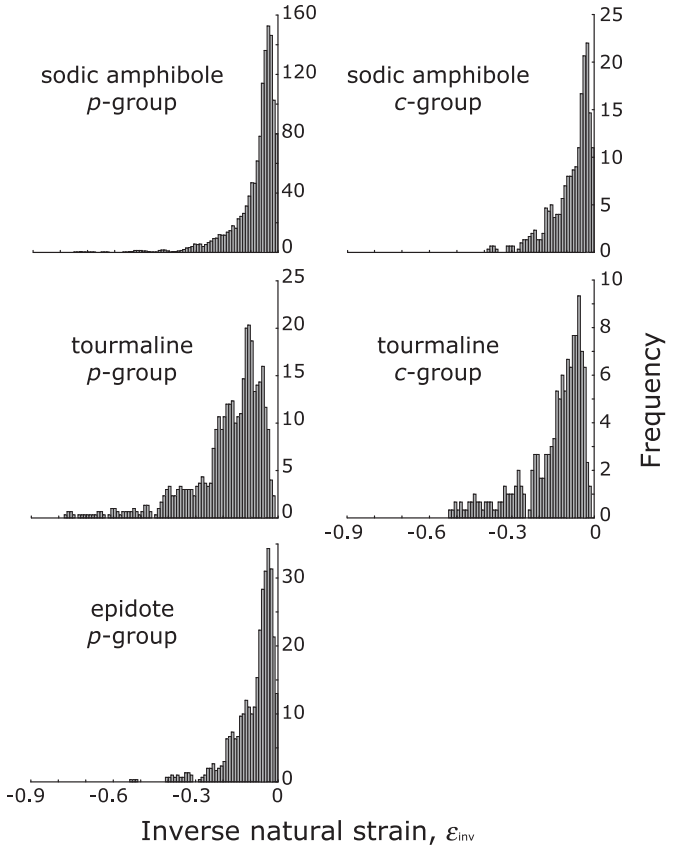

Fig. 10. Frequency distribution of fracturing with respect to inverse natural strain (ε_{inv}, with steps of 0.01) for sodic amphibole (p- and c-orientations), tourmaline (p- and c-orientations), and epidote (p-orientation).

respectively; $r_i = i - 0.5$; and N is the number of measurement points. The value of λ is then determined to minimise $T(\lambda)$ with a weighting $h(r_i)$. This procedure is equivalent to obtaining the best-fit curve between $G(r_i,\lambda)$ and $M(r_i)$.

Following Kasper and Lonslade (1967, p. 330), the standard deviation of the λ-value ($\Delta\lambda$) is calculated by

$$\Delta\lambda = \sqrt{\frac{1}{N-1}\frac{\sum_{i=1}^{N} h(r_i)[M(r_i) - G(r_i,\lambda)]^2}{\sum_{i=1}^{N} h(r_i)\left(\frac{\partial G(r_i,\lambda)}{\partial\lambda}\right)^2}}, \tag{22}$$

where

$$\frac{\partial G(r_i,\lambda)}{\partial\lambda} = -2C(r_i)\lambda\exp\left(C(r_i)\lambda^2\right) \tag{23}$$

and

$$C(r_i) = -\frac{1}{2}r_i\left(\frac{E_f}{E_q}\right)^2\left\{1 - \left(1 - \frac{E_q}{E_f}\right)\frac{1}{\cosh(Ar_i)}\right\}^2. \tag{24}$$

For the derivation of Eq. (22), see Appendix 2.

Fig. 8 shows the calculated stress parameter λ and its standard deviation for each of the four groups and the best-fit curves at four representative values of ε_{inv}.

The above method for determining the values of λ and their $\Delta\lambda$ is superior to that adopted in Masuda et al. (2003), because the latter method cannot evaluate $\Delta\lambda$. The values of λ obtained using the two methods are basically the same (within ± 0.01).

5. Result of the size-effect model on fracturing in amphibole

In a $\log(\lambda_X/\lambda_D)$ versus $\log(\overline{w_X}/\overline{w_D})$ diagram at each representative value of ε_{inv} (Fig. 9), one point can be plotted for group A with respect to group D by substituting appropriate λ_X/λ_D and $\overline{w_X}/\overline{w_D}$ values. In a similar manner, amphibole grains of group B and C can be compared with those of group D. The three straight lines in Fig. 9 are drawn for the three size-effect models with the tangent z/m. From this figure, the most suitable size-effect model for amphibole grains ($m = 2$) is the effective-length model with $z = 1$. Thus, from Eq. (16) we derive a general formula:

$$S^* = S_0^*\left(\frac{1}{\overline{w}}\right)^{1/2}, \tag{25}$$

where $\overline{w}$ is the mean width in millimetres, S^* is the modal fracture strength of a group of amphibole grains with width $\overline{w}$ and S_0^* is the standard value of S^* at $\overline{w} = 1$ mm.

6. Fundamental equation for S_0^* of amphibole

The above result demonstrates that the size effect on fracture strength for sub-millimetre-scale amphibole grains is well represented by the effective-length model. This conclusion is consistent with the findings of Kimura et al. (2006), who reported that the effective-length model (e.g., Matsuo et al., 1987) is the most suitable model for tourmaline and epidote, based on geological constraints. Thus, Eq. (25) is equally applicable to tourmaline and epidote as it is to amphibole. Equation (1) is then rewritten as follows for each of these three minerals:

$$\sigma_0 = \lambda_a S_{a0}^*\left(\frac{1}{\overline{w_a}}\right)^{1/2}, \tag{26}$$

$$\sigma_0 = \lambda_t S_{t0}^*\left(\frac{1}{\overline{w_t}}\right)^{1/2}, \tag{27}$$

and

$$\sigma_0 = \lambda_e S_{e0}^*\left(\frac{1}{\overline{w_e}}\right)^{1/2}, \tag{28}$$

where the suffixes a, t, and e denote amphibole, tourmaline, and epidote, respectively.

Here, we note the following points.

(1) σ_0 is considered to have a common value in the three equations above if the microboudinage analysis is performed on minerals within a single sample. The Eskisehir metachert considered in the present study is therefore an excellent sample for such an analysis.
(2) λ_a, λ_t, and λ_e can be determined by microboudinage analysis.
(3) $\overline{w_a}, \overline{w_t}$, and $\overline{w_e}$ can be measured.
(4) S_{a0}^*, S_{t0}^*, and S_{e0}^* are unknown.
(5) Recently, Masuda et al. (2008) proposed an equation that describes the relationship between instantaneous-fracture strength (S_0^{**}) and fatigue strength (S_0^*) for tourmaline:

$$S_0^* = S_0^{**}\frac{K_0}{K_C} \tag{29}$$

where K_0 and K_C are the subcritical growth limit (fatigue limit) and fracture toughness, respectively. Then, Eqs. (26)–(28) are rewritten as

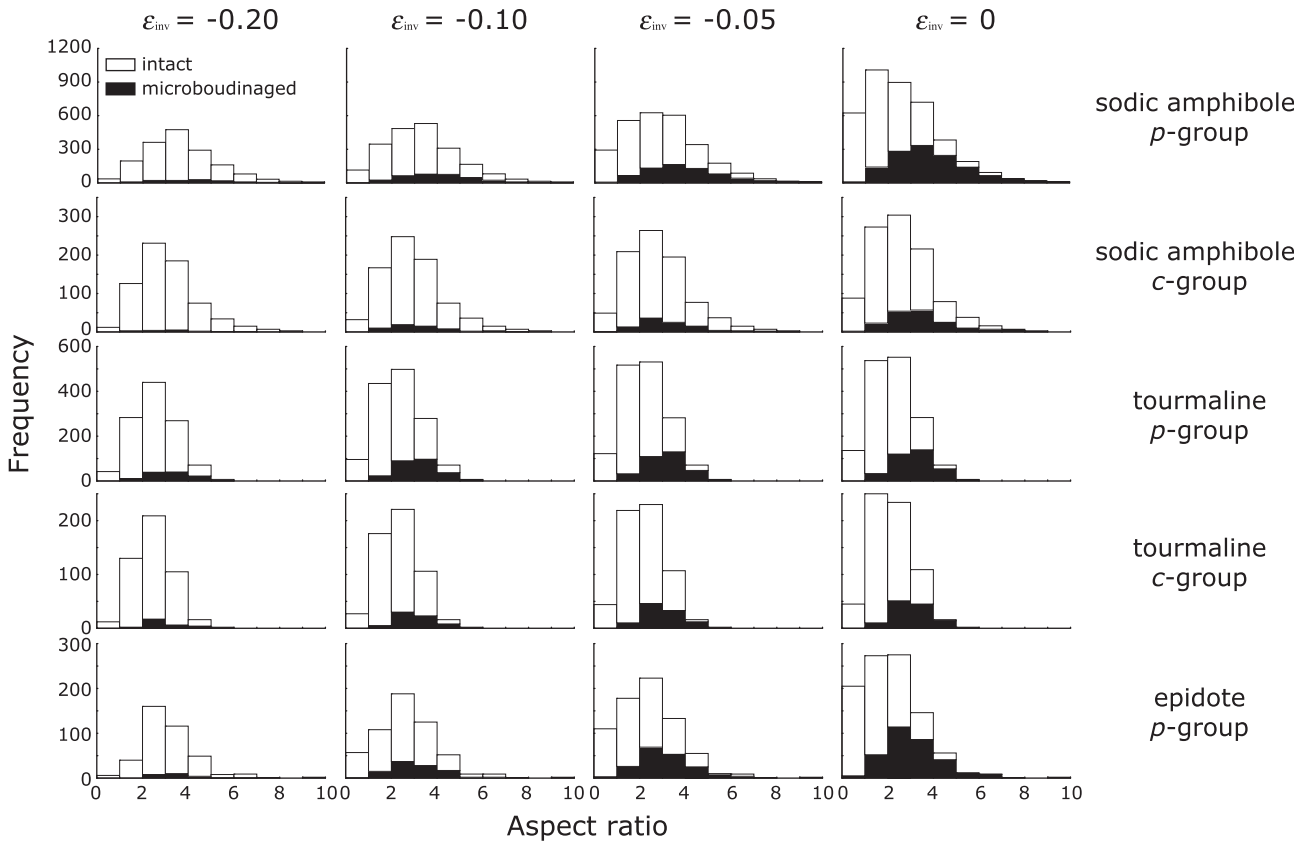

Fig. 11. Frequency distribution of microboudinaged (black) and intact grains (white) with respect to aspect ratio for sodic amphibole (*p*- and *c*-orientations), tourmaline (*p*- and *c*-orientations), and epidote (*p*-orientation) at $\varepsilon_{inv} = 0$, −0.05, −0.10, and −0.20.

$$\sigma_0 = \lambda_a S^{**}_{a0} \frac{K_{a0}}{K_{aC}} \left(\frac{1}{\overline{w_a}}\right)^{1/2}, \tag{30}$$

$$\sigma_0 = \lambda_t S^{**}_{t0} \frac{K_{t0}}{K_{tC}} \left(\frac{1}{\overline{w_t}}\right)^{1/2} \tag{31}$$

and

$$\sigma_0 = \lambda_e S^{**}_{e0} \frac{K_{e0}}{K_{eC}} \left(\frac{1}{\overline{w_e}}\right)^{1/2}, \tag{32}$$

respectively. In these equations, the suffixes *a*, *t*, and *e* again denote amphibole, tourmaline, and epidote, respectively.

(6) Although the instantaneous-fracture strength for amphibole (S^{**}_{a0}) is unknown, those for tourmaline (S^{**}_{t0} = 39 MPa) and epidote (S^{**}_{e0} = 64 MPa) were experimentally determined by Kimura et al. (2006).

(7) Here, we assume that the K_0/K_C value is common for amphibole, tourmaline, and epidote. Then, from Eqs. (30) and (31) we have

$$S^{**}_{a0} = 39 \frac{\lambda_t}{\lambda_a} \left(\frac{\overline{w_a}}{\overline{w_t}}\right)^{1/2}, \tag{33}$$

and from Eqs. (30) and (32) we have

$$S^{**}_{a0} = 64 \frac{\lambda_e}{\lambda_a} \left(\frac{\overline{w_a}}{\overline{w_e}}\right)^{1/2}. \tag{34}$$

These equations indicate that S^{*}_{a0} can be calculated when we know the values of $\overline{w_a}, \overline{w_t}, \overline{w_e}$, λ_a, λ_t, and λ_e.

7. Determination of $\overline{w_a}, \overline{w_t}, \overline{w_e}$, λ_a, λ_t, and λ_e

The values of $\overline{w_a}, \overline{w_t}, \overline{w_e}$, λ_a, λ_t, and λ_e can be determined via microboudinage analysis (i.e., the same procedure as that described in Sections 4.1–4.5). In this analysis, we analysed *p*- and *c*-orientation sodic amphibole and tourmaline grains, and *p*-orientation epidote grains (Figs. 1 and 2). The *p*-orientation microboudins are considered to have developed under the influence of $\sigma_1 - \sigma_3$, and those in *c*-orientation are considered to have developed under the influence of $\sigma_1 - \sigma_2$ (Fig. 1a). The values of $\overline{w_a}, \overline{w_t}, \overline{w_e}$, λ_a, λ_t, and λ_e can be determined independently for each mineral in each orientation (i.e., for grains in each group).

7.1. Basic data for the microboudinage technique

Among *p*-orientation crystals, we measured 1428 grains of sodic amphibole, 884 of tourmaline, and 343 of epidote. Among *c*-orientation crystals, we measured 656 grains of amphibole and 416 of tourmaline. The reliability of the obtained λ-value is strongly dependent on the number of measured grains (i.e., the reliability increases with increasing number of grains). In the above analysis of the various size-effect models (Section 4.2), we divided amphibole grains into six groups based on their width. In the present analysis, in contrast, we deal with all of the measured grains of each mineral species (for *p*- and *c*-orientations) as a single group to maximise the number of measured grains.

To reconstruct the microboudinage history, the frequency distribution of fracturing with respect to ε_{inv} is calculated based on the strain reversal method (see Section 4.3 for details) for the three analysed minerals (Fig. 10). Once the microboudinage history has been determined, the frequency distributions of values of aspect

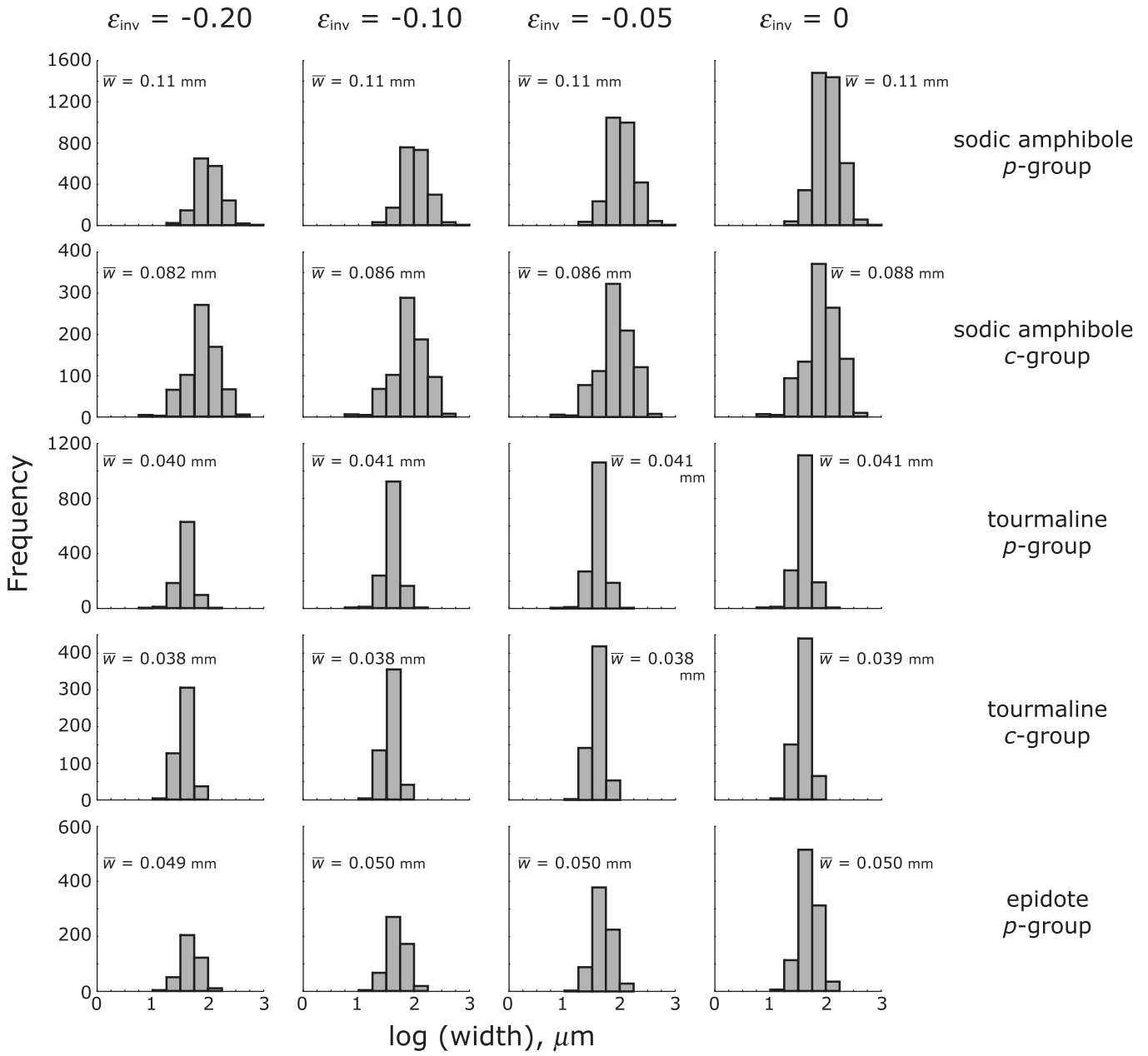

Fig. 12. Frequency distribution of the width of sodic amphibole (*p*- and *c*-orientation grains), tourmaline (*p*- and *c*-orientations), and epidote (*p*-orientation) at $\varepsilon_{inv} = 0$, −0.10, and −0.20. $\overline{w}$ indicates the geometric mean width of the grains.

ratio and width for intact and microboudinaged grains can be calculated at any given value of ε_{inv} (Figs. 11 and 12).

Fig. 13 shows the calculated stress parameter λ and its standard deviation for the three analysed minerals (λ_a, λ_t, and λ_e) and the best-fit curves at four representative values of ε_{inv} (0, −0.05, −0.10, and −0.20) in each orientation. In Eq. (20), E_f/E_q values of 1.2, 2.0, and 1.6 are used for sodic amphibole, tourmaline, and epidote, respectively, along with A_0 values of 0.6, 0.4, and 0.5 (see Section 4.5 for details).

7.2. Changes in stress parameters (λ_a, λ_t, and λ_e) and grain size data ($\overline{w}_a, \overline{w}_t$, and $\overline{w}_e$) with respect to ε_{inv}

Fig. 14 shows the obtained stress parameters and grain size data for the three analysed minerals with respect to ε_{inv}. All three minerals show a gradual increase in λ-value approaching $\varepsilon_{inv} = 0$ (cessation of plastic deformation). From Eq. (1), the λ-value is interpreted as an indicator of the relative stress magnitude within a given mineral species. As the microboudinage event considered in this study occurred during exhumation-related retrograde metamorphism (see Masuda et al., 2007), these data clearly demonstrate that differential stress increased with decreasing metamorphic temperature and pressure.

8. Determination of S^{**}_{a0}

The value of S^{**}_{a0} can be calculated by Eqs. (33) and (34) using the six parameters described in the previous section. The only prerequisite for the use of these equations is that the stress parameters and grain size data for the different mineral species should be calculated for a single, common time period. The timing can be evaluated based on the value of ε_{inv}, as the separation of newly formed microboudins is not dependent on mineral species.

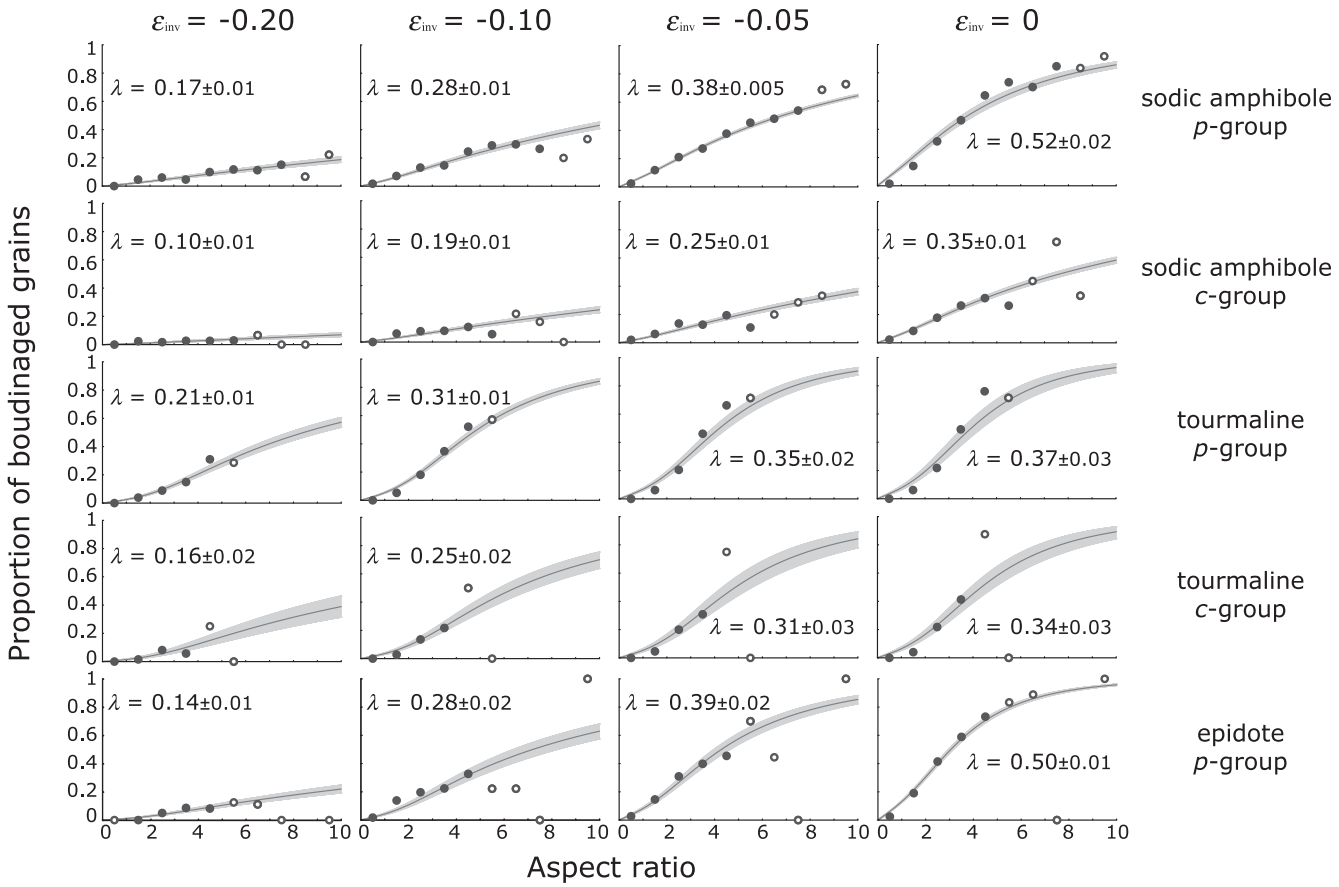

Fig. 13. Proportion of boudinaged grains (relative to the total number of grains) with respect to aspect ratio at $\varepsilon_{inv} = 0$, -0.05, -0.10, and -0.20. Also shown are the values of λ and its standard deviation for sodic amphibole, tourmaline, and epidote in each group. For additional explanations of solid and open circles, solid lines, and shaded areas, see Fig. 8.

The one factor that requires care in this regard is the separation direction of the microboudins: the same ε_{inv} value for different orientations does not indicate synchronous timing, because the strain (separation) rate is dependent on orientation. Fig. 15 shows the relation between λ-values for sodic amphibole and those for tourmaline and epidote, for two orthogonal orientations (parallel and perpendicular to the lineation, upon the foliation surface). Because the ratio of fracture strength for two different columnar minerals does not depend on the orientation of mineral grains, S_{a0}^{**} values calculated from *p*- and *c*-orientation tourmaline data can be plotted on the same abscissa.

Fig. 16 shows S_{a0}^{**} values obtained for *p*- and *c*-orientation tourmaline (using Eq. (33)) and *p*-orientation epidote (using Eq. (34)) plotted with respect to λ_a. Because microboudinage data for sodic amphibole and tourmaline were obtained for two orthogonal orientations (*p*- and *c*-orientations), S_{a0}^{**} values can be calculated separately for the two orientations. Fig. 16 shows that S_{a0}^{**} is not strongly dependent on λ_a or the orientation of mineral grains. In the present study, S_{a0}^{**} is estimated to be 80 MPa (as a representative value), with an uncertainty of ±25% (a discussion of the representative value for S_{a0}^{**} is provided below).

9. Discussion

9.1. Site of critical microcracks

The applicability of the effective-length model suggests that critical microcracks from which fracturing initiates are located on the edges of the columnar grains. According to the literature on ceramics (e.g., Davidge, 1979; Awaji, 2001), the effective-surface model is applied when critical microcracks are induced on the surface of rectangular test pieces during preparation, whereas the effective-volume model is preferable when the ceramic test pieces are carefully polished to eliminate surface microcracks. However, the origin of microcracks on the edges of test specimens has received little attention in materials science, and the effective-length model is only dealt with in Matsuo et al. (1987). A degree of interpretation is therefore required to explain the presence of critical microcracks on the edges of columnar amphibole grains.

Because the microboudinage of amphibole occurs during the final stages of metamorphism, prior to the cessation of plastic flow of quartz at the plastic–brittle transition (e.g., Masuda et al., 2007), critical microcracks such as those described above should be present during the exhumation stage, before the initiation of microboudinage. The microcracks could therefore potentially form during either the growth stage or the post-growth stage of the minerals of interest; however, microcracks are considered unlikely to develop during the growth stage because they possess excess surface energy, and the surface diffusion of elements would proceed to eliminate such excess energy. The likelihood that microcracks are induced during the post-growth stage is considered below.

When amphibole growth ceases at high pressures and temperatures, the crystal lattice at the surface of the grain must adjust coherently to the lattices of surrounding quartz grains. Because amphibole and quartz have different thermal expansion coefficients and linear elastic constants (e.g., Nye, 1957; Clark, 1966; Simmons and Wang, 1971), a simultaneous decrease in temperature and pressure during exhumation will cause a misfit along the boundaries between amphibole and quartz grains. This misfit leads

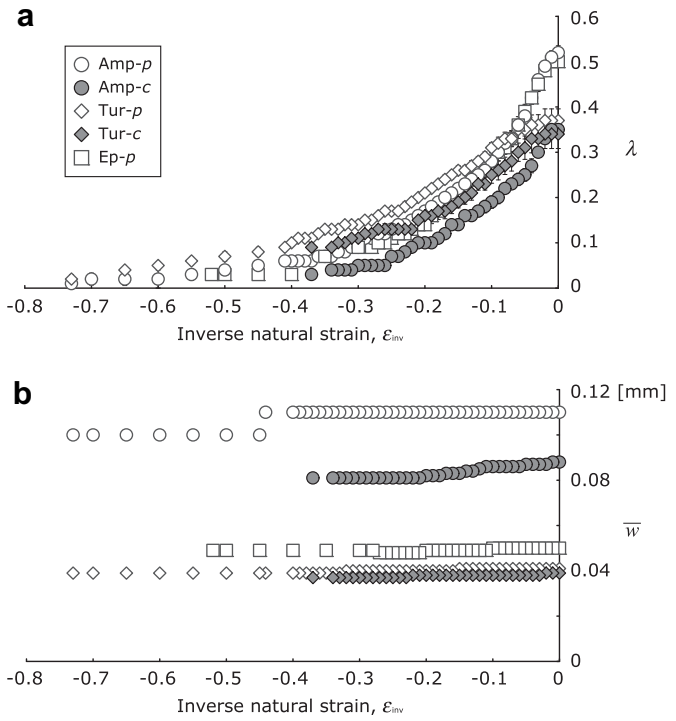

Fig. 14. λ-values for sodic amphibole, tourmaline, and epidote for each orientation (a) and the geometric mean width of grains ($\overline{w}$) for these minerals (b) with respect to inverse natural strain (ε_{inv}). The error bars for λ-values are smaller than the sizes of the symbols when the standard deviation is below 0.02. Amp-p = sodic amphibole in p-orientations. Amp-c = sodic amphibole in c-orientations. Tur-p = tourmaline in p-orientations. Tur-c = tourmaline in c-orientations. Ep-p = epidote in p-orientations.

in turn to local strain and subsequently a local increase in stress along coherent grain boundaries. As the thermal expansion coefficient and linear elastic constant are anisotropic with respect to the crystallographic axes of amphibole and quartz (e.g., Nye, 1957), strain is presumably heterogeneously distributed upon the various crystal faces of individual amphibole grains. The local stress will therefore concentrate along the edges of amphibole grains in a complicated manner, depending on the nature of the decrease in temperature and pressure and the crystallographic orientations of the amphibole and surrounding quartz grains. Given that amphibole grains must inevitably contain micropores, microinclusions, fluid inclusions, surface jogs, asperities, and other crystalline defects on their edges or close to their edges, such a stress concentration will interact with these defects to selectively generate microcracks along the edges of the crystals. The non-hydrostatic far-field stress state may also enhance this stress concentration by enhancing the anisotropy of the misfit.

9.2. Value of S_{a0}^{**}

The calculation of S_{a0}^{**} via Eq. (33) should ideally yield the same value as that calculated using Eq. (34); however, the values of S_{a0}^{**} estimated from tourmaline and epidote data (Fig. 16) are only consistent within the range of $0.10 \le \lambda_a \le 0.24$: values of S_{a0}^{**} at $\lambda_a < 0.10$ are unstable, while those at $\lambda_a > 0.24$ show a gradual divergence with increasing λ_a. This divergence is considered to reflect the dissimilar response of tourmaline to fracturing compared with that of the other two minerals. In Fig. 14a, the change in λ_t with respect to ε_{inv} shows a different trend than that for λ_a and λ_e, especially at $\varepsilon_{inv} = 0$ to -0.06 in the p-orientation and $\varepsilon_{inv} = 0$ to -0.04 in the c-orientation. This tendency is more prominent in Fig. 15, in which tourmaline data show a change in trend at $\lambda_a \approx 2.7$.

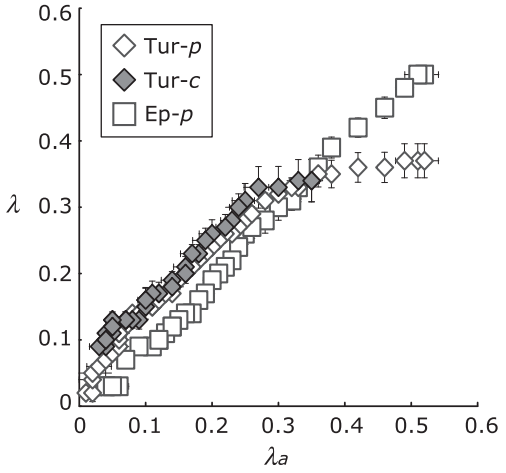

Fig. 15. Relations among λ-values for sodic amphibole (λ_a), tourmaline, and epidote for each orientation. See Fig. 14 for an explanation of error bars and symbols.

Because λ_a is given with reference to plastic strain (for all three minerals, λ increases with increasing ε_{inv}; Fig. 14a) and the microboudinage event occurred during a period of decreasing temperature and pressure (i.e., during exhumation; see Masuda et al., 2007), the divergence shown in Fig. 16 may be related to the dissimilar responses of the three mineral species to these conditions. In the present study, as we have no reliable data on the pressure and temperature dependences of the fracture strength of the considered minerals, we propose a representative values of S_{a0}^{**} of 80 MPa, with an uncertainty of ±25%. This value will be refined in future studies.

10. Equation for palaeostress analysis using amphibole microboudinage structures

The value of S_{a0}^{**} (=80 MPa) derived from Eqs. (33) and (34) is based on the premise of instantaneous fracturing of amphibole grains (i.e., crack velocity exceeding 10^{-2} m/s; e.g., Weaver, 1984) during the development of microboudinage structures. In contrast, observations of fatigue fracturing during slow crack growth ($<10^{-9}$ m/s; e.g., Weaver, 1984; Scholz, 2002) have been reported from naturally deformed rocks (e.g., Barnett and Kerrich, 1980; Kanaori, 1983). When fatigue fracturing occurs, the magnitude of fracture strength shows a marked reduction compared with that under instantaneous fracturing (e.g., Weaver, 1984; Atkinson, 1987; Blenkinsop, 1996; Scholz, 2002; Paterson and Wong, 2005).

Masuda et al. (2008) tentatively assumed a K_{t0}/K_{tC} value of 0.1, for tourmaline based on the literature for ceramics and glass (e.g., Weaver, 1984; Sglavo and Green, 1996). In the present study, we follow this value when considering amphibole; accordingly, we assume $K_{a0}/K_{aC} = 0.1$. Given that $S_{a0}^{**} = 80$ MPa, Eq. (30) is rewritten as a function of the stress parameter (λ_a) and mean grain width ($\overline{w_a}$):

$$\sigma_0 = 8\lambda_a \left(\frac{1}{\overline{w_a}}\right)^{1/2}. \tag{35}$$

This equation therefore provides a measure of the far-field palaeodifferential stress based on amphibole microboudinage structures.

11. Geological significance of amphibole microboudinage structures

Monomineralic rocks such as metachert and marble, which occasionally yield microboudinaged columnar amphibole grains, are found over a wide range of geological ages and metamorphic

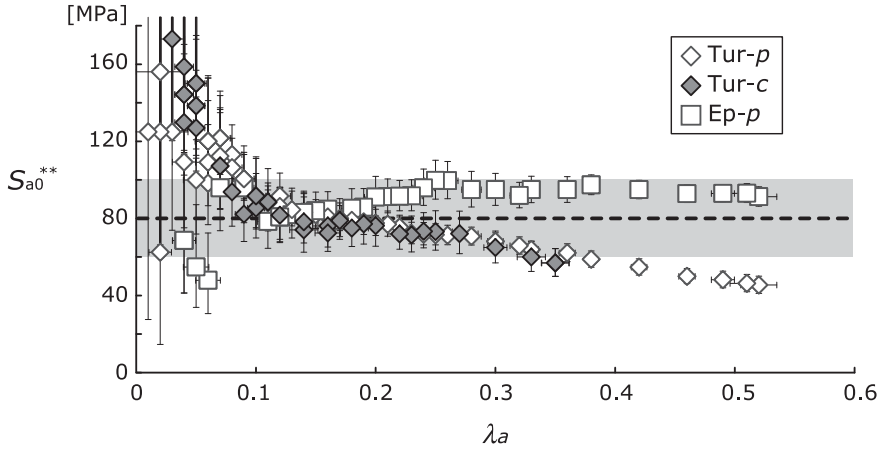

Fig. 16. Estimated value of S_{a0}^{**} with respect to λ-values for sodic amphibole (λ_a) based on an analysis of sodic amphibole (p- and c-orientations), tourmaline (p- and c-orientations), and epidote (p-orientation). The representative value of S_{a0}^{**} (=80 MPa) and its 25% deviation are indicated by the dashed line and shaded region, respectively. The estimated range of S_{a0}^{**} (note: this value is not equal to the error bar) indicated by the solid bars is calculated from the standard deviation of λ for the three minerals. For an explanation of the symbols, see Fig. 14.

conditions. For example, metacherts from the 3800 Ma Isua supracrustal belt, Greenland, contain microboudins of columnar grunelite and cummingtonite (author's observation (T. Masuda)), while Tertiary Alpine metamorphic rocks contain microboudins of sodic amphibole in metachert (e.g., Mottana, 1986; Passchier and Trouw, 2005). Metacherts in high-pressure/temperature metamorphic belts also contain microboudins of columnar sodic amphibole (e.g., Misch, 1969; Helper, 1986; Parkinson, 1998; Masuda et al., 2004a,b), while calcareous rocks within the aureole of the Main Donegal Granite, Ireland, contain microboudins of tremolite within a calcite matrix (author's observation (N. Kimura)).

The amphibole group of minerals shows a wide variety of chemical compositions, the effects of which should be taken into account to obtain more realistic estimates of fracture strength. The influence of amphibole composition on fracture strength remains unknown, and the value of S_{a0}^{*} (=8 MPa) utilises a representative value as a first approximation. Thus, Eq. (35) extends the applicability of microboudin palaeostress analysis, providing a useful tool for advanced geodynamics research.

Acknowledgements

The authors thank Kumiko Onodera for collection of the metachert sample analysed in this study, Mutsuki Aoya for a helpful review of an early version of the manuscript, and Nobuaki Niitsuma, Toshiyuki Hashida, and Hideo Awaji for their encouraging suggestions. We also thank Hideki Mori for assistance in the preparation of thin sections, Tom Blenkinsop, Oliver Lacombe, and Shaocheng Ji for constructive comments on an early version of the manuscript, and two anonymous referees for encouraging comments on the manuscript. This study was financially supported by the Japanese Society of the Promotion of Science (JSPS).

Appendix 1. Geometric mean of grain size

Fracture strength is described in a statistical manner because different pieces of a given material have different fracture strengths, even for equivalent sizes (e.g., Epstein, 1948; Weibull, 1951; Davidge, 1979; Lawn, 1993; Awaji, 2001). The parameters $S_{w_i}^{*}$ and S_0^{*} are introduced to represent the modal fracture strength of cubes with a specific width of w_i and a standard value of $S_{w_i}^{*}$ at $w_i = 1$ mm, respectively. According to the size-effect models, we derive

$$\frac{S_{w_i}^{*}}{S_0^{*}} = \left(\frac{1}{w_i}\right)^{z/m}, \tag{36}$$

where $z = 1$, 2, and 3 correspond to the effective-length, effective-area, and effective-volume models, respectively.

Consider an ideal group of grains in which all the constituent grains at a width of w_i ($i = 1$ to n) have a fracture strength equal to the modal fracture strength for grains of size $S_{w_i}^{*}$. The geometric mean of $S_{w_i}^{*}$ is defined by $\overline{S^{*}}$ as follows:

$$\overline{S^{*}} = \left(\prod_{i=1}^{n} S_{wi}^{*}\right)^{1/n}. \tag{37}$$

This equation is equivalent to

$$\log\ \overline{S^{*}} = \frac{1}{n}\sum_{i=1}^{m} \log\ S_{wi}^{*}. \tag{38}$$

Equation (36) leads to

$$\log\ S_{wi}^{*} - \log\ S_0^{*} = -\frac{z}{m}(\log\ w_i). \tag{39}$$

Substituting this result into Eq. (38) yields

$$\log\ \overline{S^{*}} = \frac{1}{n}\sum_{i=1}^{n}\left(\log\ S_0^{*} - \frac{z}{m}\log\ w_i\right). \tag{40}$$

Then, because S_0^{*} is a constant, we have

$$\frac{1}{n}\sum_{i=1}^{n}\log\ S_0^{*} = \log\ S_0^{*}, \tag{41}$$

and

$$\frac{1}{n}\sum_{i=1}^{n}\left(-\frac{z}{m}\log\ w_i\right) = -\frac{z}{m}\frac{1}{n}\log\left(\prod_{i=1}^{n} w_i\right). \tag{42}$$

As the geometric mean of w_i ($i = 1$ to n) is defined by $\overline{w}$ as

$$\overline{w} = \left(\prod_{i=1}^{n} w_i\right)^{1/n}, \tag{43}$$

we derive

$$\log\ \overline{S^*} - \log\ S_0^* = -\frac{z}{m}\log\ \overline{w}, \tag{44}$$

which is equivalent to

$$\frac{\overline{S^*}}{\overline{S_0^*}} = \left(\frac{1}{\overline{w}}\right)^{z/m}. \tag{45}$$

This equation appears consistent with Eq. (36). $S^*_{w_i}$ and w_i in Eq. (36) are replaced by the geometric means of $S^*_{w_i}(=\overline{S^*})$ and $w_i(=\overline{w})$ in Eq. (45), respectively.

Because the fracture strength of a grain at w_i is not always equal to $S^*_{w_i}$, the modal fracture strength of a group of grains (S^*) is not equivalent to that of the ideal case ($\overline{S^*}$); however, $S^* \approx \overline{S^*}$ is expected to be satisfied as a first approximation in the case that the group contains a large number of grains (n).

The representative value of S^* for grains of group A with width $w_{A_i}(i = 1\ \text{to}\ n)$ is defined as S^*_A, and is given by

$$\frac{S_A^*}{S_0^*} = \left(\frac{1}{\overline{w_A}}\right)^{z/m}, \tag{46}$$

where $\overline{w_A}$ is defined as the geometric mean of w_{A_i}:

$$\overline{w_A} = \left(\prod_{i=1}^{n} w_{A_i}\right)^{1/n}. \tag{47}$$

Similarly, S^*_B for group B with grain size $w_{B_i}(i = 1\ \text{to}\ n)$ is obtained as

$$\frac{S_B^*}{S_0^*} = \left(\frac{1}{\overline{w_B}}\right)^{z/m}. \tag{48}$$

From Eqs. (46) and (48), we derive Eq. (16) in the main text.

The above derivation is only possible when the geometric mean is adopted for the mean width and the mean fracture strength. A consistent equation cannot be derived using the arithmetic mean.

Appendix 2. Derivation of the equation used in calculating the standard deviation of λ

The variance of all the data (s^2) is given by

$$s^2 = \frac{1}{n-1}\sum_{i=1}^{N} h(r_i)[M(r_i) - G(r_i,\lambda)]^2, \tag{49}$$

where n is the total number of measured grains; r_i is the aspect ratio of columnar grains, given as $r_i = i - 0.5(i = 1\ \text{to}\ N)$; N is the number of measurement points, equivalent to the points plotted in Figs. 8 and 13; $h(r_i)$ is the number of measured grains at each r_i; and $M(r_i)$ and $G(r_i,\lambda)$ are the measured and theoretically predicted proportions of microboudinaged grains at r_i, respectively. Following Kasper and Lonsdale (1967), the weighted standard deviation of $G(r_i,\lambda)$ at each measurement point ($\Delta G(r_i,\lambda)$) is calculated by

$$\Delta G(r_i,\lambda) = \frac{s}{\sqrt{h(r_i)}} = \sqrt{\frac{1}{(N-1)h(r_i)}\sum_{i=1}^{N} h(r_i)[M(r_i) - G(r_i,\lambda)]^2}, \tag{50}$$

while the standard deviation of the λ-value at each measurement point ($\Delta\lambda(r_i)$) is described by

$$\Delta\lambda(r_i) = \frac{\partial\lambda}{\partial G(r_i,\lambda)}\Delta G(r_i,\lambda). \tag{51}$$

Since the standard deviation of the λ-value ($\Delta\lambda$) is given by

$$\frac{1}{(\Delta\lambda)^2} = \sum_{i=1}^{N}\frac{1}{(\Delta\lambda(r_i))^2}, \tag{52}$$

by substituting Eqs. (50) and (51) into Eq. (52), $\Delta\lambda$ is finally calculated by Eq. (22). In the above derivation, we assumed a Gaussian distribution for $M(r_i)$ with respect to $G(r_i,\lambda)$.

References

Atkinson, B.K., 1987. Fracture Mechanics of Rock. Academic Press, London.

Awaji, H., 2001. Strength of Ceramic Materials. Corona Publishing, Tokyo (in Japanese).

Barnett, R.L., Kerrich, R., 1980. Stress corrosion cracking of biotite and feldspar. Nature 283, 185–187.

Blenkinsop, T.G., 1996. Deformation Microstructures and Mechanisms in Minerals and Rocks. Kluwer Academic Publishers, Netherlands.

Burkhard, M., 1993. Calcite twins, their geometry, appearance and significance as stress–strain markers and indicators of tectonic regime: a review. Journal of Structural Geology 15, 351–368.

Clark Jr., S.P. (Ed.), 1966. Handbook of Physical Constants. Geological Society of America, New York.

Davidge, R.W., 1979. Mechanical Behaviour of Ceramics. Cambridge University Press, London.

Epstein, B., 1948. Statistical aspects of fracture problems. Journal of Applied Physics 19, 140–147.

Ernst, W.G., 1968. Amphiboles: Crystal Chemistry, Phase Relations and Occurrence. Springer-Verlag, Berlin.

Ferguson, C.C., 1981. A strain reversal method for estimating extension from fragmented rigid inclusions. Tectonophysics 79, T43–T52.

Goscombe, B.D., Passchier, C.W., Hand, M., 2004. Boudinage classification: end-member boudin types and modified boudin structures. Journal of Structural Geology 26, 739–763.

Helper, M.A., 1986. Deformation and high P/T metamorphism in the central part of the Condrey Mountain window, north-central Klamath Mountains, California and Oregon. In: Blueschists and Eclogites. Geological Society of America Memoir 164, 125–141.

Jamison, W.R., Spang, J.H., 1976. Use of calcite twin lamellae to infer differential stress. Geological Society of America Bulletin 87, 868–872.

Kanaori, Y., 1983. Fracturing mode analysis and relative age dating of faults by surface textures of quartz grains from fault gouges. Engineering Geology 19, 261–281.

Kasper, J.S., Lonsdale, K., 1967. International Tables for X-ray Crystallography. In: Mathematical Tables, second ed., vol. II. Kynoch Press, Birmingham.

Kimura, N., Awaji, H., Okamoto, M., Matsumura, Y., Masuda, T., 2006. Fracture strength of tourmaline and epidote by three-point bending test: application to microboudin method for estimating absolute magnitude of palaeodifferential stress. Journal of Structural Geology 28, 1093–1102.

Kohlstedt, D.L., Weathers, M.S., 1980. Deformation-induced microstructure, palaeopiezometers and differential stresses in deep eroded fault zone. Journal of Geophysical Research 85, 6269–6285.

Küster, M., Stöckhert, B., 1999. High differential stress and sublithostatic pore fluid pressure in the ductile regime-microstructural evidence for short-term post-seismic creep in the Sesia zone, Western Alps. Tectonophysics 303, 263–277.

Lacombe, O., 2007. Comparison of paleostress magnitudes from calcite twins with contemporary stress magnitudes and frictional sliding criteria in the continental crust: mechanical implications. Journal of Structural Geology 29, 86–99.

Lawn, B., 1993. Fracture of Brittle Solids, second ed. Cambridge University Press, Cambridge.

Leake, B.E., 1968. A Catalog of Analyzed Calciferous and Subcalciferous Amphiboles together with their Nomenclature and Associated Mineral. Geological Society of America, Boulder.

Leake, B.E., Woolley, A.R., Arps, C.E.S., Birch, W.D., Gilbert, M.C., Grice, J.D., Hawthorne, F.C., Kato, A., Kisch, H.J., Krivovichev, V.G., Linthout, K., Laird, J., Mandarino, J., Maresch, W.V., Nickel, E.H., Rock, N.M.S., Schumacher, J.C., Smith, D.C., Stephenson, N.C.N., Ungaretti, L., Whittaker, E.J.W., Youzhi, G., 1997. Nomenclature of amphiboles report of the subcommittee on amphiboles of the International Mineralogical Association Commission on new minerals and mineral names. European Journal of Mineralogy 9, 623–651.

Lloyd, G.E., Condliffe, E., 2003. 'Strain Reversal': a Windows™ program to determine extensional strain from rigid–brittle layers or inclusions. Journal of Structural Geology 25, 1141–1145.

Masuda, T., Kimura, N., Fu, B., Li, X., 2004a. Validity of the microboudin method for palaeo-stress analysis of metamorphic tectonites: application to extraordinarily

long sodic amphibole grains in a metachert from Aksu, China. Journal of Structural Geology 26, 203–206.
Masuda, T., Nakayama, S., Kimura, N., Onodera, K., Okamoto, A., 2004b. Triaxial stress state deep in orogenic belts: an example from Turkey. Journal of Structural Geology 26, 2203–2209.
Masuda, T., Kimura, N., Okamoto, A., Miyake, T., Omori, Y., 2007. Cessation of plastic deformation during exhumation of metamorphic tectonites revealed by microboudinage structures. Journal of Structural Geology 29, 159–165.
Masuda, T., Kimura, N., Hara, Y., 2003. Progress in microboudin method for palaeostress analysis of metamorphic tectonites: application of mathematically refined expression. Tectonophysics 364, 1–8.
Masuda, T., Kugimiya, Y., Aoshima, I., Hara, Y., Ikei, H., 1999. A statistical approach to determination of a mineral lineation. Journal of Structural Geology 21, 467–472.
Masuda, T., Nakayama, S., Kimura, N., Okamoto, A., 2008. Magnitude of σ_1, σ_2, and σ_3 at mid-crustal levels in an orogenic belt: microboudin method applied to an impure metachert from Turkey. Tectonophysics 460, 230–236.
Masuda, T., Shibutani, T., Igarashi, T., Kuriyama, M., 1989. Microboudin structure of piemontite in quartz schists: a proposal for a new indicator of relative palaeodifferential stress. Tectonophysics 163, 169–180.
Masuda, T., Shibutani, T., Kuriyama, M., Igarashi, T., 1990. Development of microboudinage: an estimate of changing differential stress with increasing strain. Tectonophysics 178, 379–387.
Masuda, T., Shibutani, T., Yamaguchi, H., 1995. Comparative rheological behavior of albite and quartz in siliceous schists revealed by the microboudinage of piedmontite. Journal of Structural Geology 17, 1523–1533.
Matsuo, Y., Ogasawara, T., Kimura, S., Yasuda, E., 1987. Statistical analysis of the effect of surface grinding on the strength of alumina using Weibull's multimodal function. Journal of Materials Science 22, 1482–1488.
Mercier, J.-C.C., Anderson, D.A., Carter, N.L., 1977. Stress in the lithosphere: inferences from steady state flow of rocks. Pure and Applied Geophysics 115, 199–226.
Misch, P., 1969. Paracrystalline microboudinage of zoned grains and other criteria for synkinematic growth of metamorphic minerals. American Journal of Science 267, 43–63.
Mottana, A., 1986. Blueschist-facies metamorphism of manganiferous cherts: a review of the alpine occurrence. In: Blueschists and Eclogites. Geological Society of America Memoir 164, 267–299.
Nye, J.F., 1957. Physical Properties of Crystals. Oxford University Press, Oxford.
Okay, A.I., 2002. Jadeite–chloritoid–glaucophane–lawsonite blueschists in northwest Turkey: unusually high P/T ratios in continental crust. Journal of Metamorphic Geology 20, 757–768.
Okay, A.I., Harris, N.B.W., Kelley, S.P., 1998. Exhumation of blueschists along a Tethyan suture in northwest Turkey. Tectonophysics 285, 275–299.
Ord, A., Christie, J.M., 1984. Flow stresses from microstructures in mylonitic quartzites of the Moine Thrust Zone, Assynt area, Scotland. Journal of Structural Geology 6, 639–654.
Papike, J.J., 1969. Pyroxenes and Amphiboles. Mineralogical Society of America, Menasha.
Parkinson, C., 1998. An outline of the petrology, structure and age of the Pompangeo Schist Complex of central Sulawesi, Indonesia. The Island Arc 7, 231–245.
Passchier, C.W., Trouw, R.A.J., 2005. Microtectonics, second ed. Springer-Verlag, Berlin.
Paterson, M.S., Wong, T.-f., 2005. Experimental Rock Deformation – the Brittle Field, second ed. Springer, Berlin.
Scholz, C.H., 2002. The Mechanics of Earthquakes and Faulting, second ed. Cambridge University Press, Cambridge.
Simmons, G., Wang, H., 1971. Single Crystal Elastic Constants and Calculated Aggregate Properties: a Handbook. MIT Press, Cambridge, 370 pp.
Sglavo, V.M., Green, D.J., 1996. Threshold stress intensity factor in soda-lime silicate glass by interrupted static fatigue test. Journal of European Ceramic Society 16, 645–651.
Stipp, M., Tullis, J., 2003. The recrystallized grain size piezometer for quartz. Geophysical Research Letters 30 SDE 3-1-SDE 3-5.
Twiss, R.J., 1977. Theory and applicability of a recrystallized grain size palaeopiezometer. Pure and Applied Geophysics 115, 227–244.
Twiss, R.J., 1986. Variable Sensitivity Piezometric Equations for Dislocation Density and Subgrain Diameter and their Relevance to Olivine and Quartz. In: Hobbs, B.E. and Heard, H.C. (Ed.), Mineral and rock deformation: laboratory studies. Geophysical Monograph 36. American Geophysical Union, pp. 247–261.
Veblen, D.R. (Ed.), 1981. Amphiboles; Petrology and Experimental Phase Relations. Mineralogical Society of America, Washington D.C.
Weathers, M.S., Bird, J.M., Cooper, R.F., Kohlstedt, D.L., 1979. Differential stress determined from deformation-induced microstructures of the Moine thrust zone. Journal of Geophysical Research 84, 7495–7509.
Weaver, G., 1984. Engineering with ceramics part II: life time prediction. Journal of Materials Education.
Weibull, W., 1951. A statistical distribution function of wide applicability. Journal of Applied Mechanics 22, 293–297.
White, S.H., Burrows, S.E., Carreras, J., Shaw, N.D., Humphreys, F.J., 1980. On mylonites in ductile shear zones. Journal of Structural Geology 2, 175–187.
Zhao, P., Ji, S., 1997. Refinements of shear-lag model and its applications. Tectonophysics 279, 37–53.